Impact of crystal sedimentation and viscoplastic semi-solid dynamics on macrosegregation

IOP Conf. Series: Materials Science and Engineering **861** (2020) 012042 doi:10.1088/1757-899X/861/1/012042

Impact of crystal sedimentation and viscoplastic semi-solid dynamics on macrosegregation

C M G Rodrigues[1], A Ludwig[1], M Wu[1], A Kharicha[1,2] and A Vakhrushev[1]

[1] Chair of Simulation and Modelling of Metallurgical Processes, Metallurgy Department, Montanuniversitaet Leoben, Franz-Josef Street 18, 8700 Leoben, Austria
[2] Christian-Doppler Laboratory for Metallurgical Application of Magnetohydrodynamics, Montanuniversitaet of Leoben, Franz-Josef Street 18, 8700 Leoben, Austria

E-mail: christian.gomes-rodrigues@unileoben.ac.at

Abstract. A numerical investigation of melt convection with solid-phase transport during equiaxed solidification is performed to examine the structural and compositional evolution of an Al-Si alloy. Nucleation and growth kinetic laws are coupled with the general conservation equations employed in fluid dynamics to predict the development of the solidification structure. Besides crystal sedimentation due to buoyancy-induced forces in the low solid fraction range, the model covers also the viscoplastic semi-solid dynamics at high solid fractions. A test case is devised such that two viscoplastic structures grow from the vertical walls towards the centre of the domain and eventually merge at an arbitrary distance from the bottom of a simple cavity setup. This introduces difficulties for the solidification-driven feeding flow which has been associated with pressure drops across the domain. Dilatation of the mush is also predicted in the lower part of the solidifying viscoplastic mush, which means that additional melt is drawn to this area. Interestingly, besides liquid feeding, also a significant amount of solid feeding has been detected to compensate for solidification shrinkage. Such synergetic behaviour between the phases is analysed in terms of macrosegregation.

1. Introduction

In the last decades, solidification has evolved from a purely industrial-driven activity to a science-based field. Numerous fundamental developments have been achieved in recent years and the understanding of the underlying physics during a phase change has increased greatly from both analytical and experimental studies. However, industry has also coped with today's technological competitiveness by building up greater reliance on computer-aided engineering, and more particularly on numerical simulations. This paradigm shift has driven the development of computational models aimed at replicating definite phenomena.

In the present paper, a two-phase Eulerian-Eulerian volume-average model is presented that simulates the transport, nucleation and growth of equiaxed crystals during solidification. The solidification spectrum is separated into two distinct regimes. At low solid fractions, the behavior of the solid-liquid mixture is described as suspensions [1], and the rheology of the mixture is mainly dictated by the transporting character of the liquid phase. At high solid fractions, on the other hand, the crystals create a coherent structure that is capable of sustaining significantly higher stresses [2]. In this regime (referred as the viscoplastic regime), the solid phase is characterized by having a dynamic behavior at

high temperatures. It is also often characterized as a solid skeleton saturated with liquid [3, 4]. Furthermore, it can also deform by shrinkage, convection or due to the application of external loads. As a result, the mush either densifies (by expelling liquid from its core) or dilates (by draining liquid from its surroundings) [3], which alters the composition of the alloy [5, 6]. Based on the experimental work of Nguyen [7], who studied the mechanical behavior of an alloy in the semi-solid state, the transition between the two regimes has been set at a solid fraction (g_s^t) of 57%.

In a previous work [8], it was found that densification or dilatation of the mush in simple cavity setups was not strong enough to induce solute redistribution. In order to gain more insight into the semi-solid dynamics in the viscoplastic regime, the configuration in the present work has been modified so that viscoplastic structures start to interact between each other more intensely, and solidification feeding requirements across the domain accentuates the effect of the semi-solid dynamics and mush deformation during the casting process. It is worth noting that the formation of porosity, which would limit locally the pressure drop, is neglected in this work.

2. Model description

The two-phase Eulerian-Eulerian volume-average model is based on the *twoPhaseEulerFoam* solver from OpenFOAM toolbox [9]. However, the original code has been greatly altered mainly to incorporate the viscoplastic regime, which was not supported by the solver. This includes (among other developments) the addition of the bulk viscosity in the viscous stress term, the adaptation of the Navier-Stokes equation to cope with the different rheological material behaviors depending on the regime, and the calculation of the effective solid viscosity as a quantity that is function of the solid fraction or the equivalent strain rate (depending on the regime). These quantities are defined in the following.

The volume-average conservation equations of mass, momentum, species, and enthalpy are solved for the liquid and the solid phases. They are presented in table 1, where g denotes the volume fraction, ρ the density, $\mathbf{v}$ the velocity vector, p the shared pressure, $\boldsymbol{\Sigma}_i^{eff}$ the effective deviatoric stress tensor, $\mathbf{g}$ the gravity vector, c the species concentration, h the enthalpy per unit mass, $\mathbf{q}$ the heat flow vector, n the grain number density, and the subscripts i refer to either liquid (ℓ) or solid (s). In each computational cell, the sum of solid and liquid volume fractions (g_s and g_ℓ, respectively) is equal to one.

Table 1. Volume-Averaged Conservation Equations.

Mass conservation:	$\frac{\partial g_i \rho_i}{\partial t} + \nabla \cdot (g_i \rho_i \mathbf{v}_i) = \mp M_{\ell s}$	(1)
Momentum conservation:	$\frac{\partial g_i \rho_i \mathbf{v}_i}{\partial t} + \nabla \cdot (g_i \rho_i \mathbf{v}_i \mathbf{v}_i) = -g_i \nabla p + \nabla \cdot g_i \boldsymbol{\Sigma}_i^{eff} + g_i \rho_i \mathbf{g} \mp \mathbf{U}_{ls}^D \mp \mathbf{U}_{ls}^M$	(2)
Species conservation:	$\frac{\partial g_i \rho_i c_i}{\partial t} + \nabla \cdot (g_i \rho_i \mathbf{v}_i c_i) = \nabla \cdot (g_i \rho_i D_i \nabla c_i) \mp C_{\ell s}$	(3)
Enthalpy conservation:	$\frac{\partial g_i \rho_i h_i}{\partial t} + \nabla \cdot (g_i \rho_i \mathbf{v}_i h_i) = -\nabla \cdot \mathbf{q}_i \mp H_{\ell s}$	(4)
Grain transport:	$\frac{\partial n}{\partial t} + \nabla \cdot (\mathbf{v}_s n) = N_{\ell s}$	(5)

The coupling between the phases is achieved through the single pressure field, p, and the different interphase exchange terms $M_{\ell s}$, $\mathbf{U}_{\ell s}$, $C_{\ell s}$, $H_{\ell s}$ and $N_{\ell s}$ which are presented in table 2. The sign of the source terms depends on the phase, with "$\mp$" being positive when $i=s$, and negative when $i=\ell$.

The quantities v_r, $S_{\ell s}$, Φ_{imp}, $K_{\ell s}$ and u^* are the crystal growth velocity, specific surface area, impingement factor, momentum exchange coefficient due to drag and momentum exchange velocity coefficient due to phase change. The enthalpy exchange term is used to satisfy the condition of thermal equilibrium between phases (with $h_c = 10^9$ W/m^2/K). The diffusion coefficient, D, in equation (3) is equal to 1.63×10^{-9} m^2/s for the liquid and 8×10^{-13} m^2/s for the solid, whereas the effective thermal diffusivity for enthalpy, α, in equation (10) is equal to 0.058 m^2/s for the liquid and 0.166 m^2/s for the solid. Further

details on the conservation equations, source terms and auxiliary equations considered in the development of the model have been described in detail in a companion paper [5].

Table 2. Exchange terms and other closure laws for the conservation equations.

mass transfer:	$M_{\ell s} = v_r S_{\ell s} \rho_s \Phi_{\text{imp}}$	(6)
momentum transfer:	$\mathbf{U}_{\ell s} = \mathbf{U}_{\ell s}^{M} + \mathbf{U}_{\ell s}^{D} = K_{\ell s}(\mathbf{v}_\ell - \mathbf{v}_s) + u^* M_{\ell s}$	(7)
species transfer:	$C_{\ell s} = c_s^* M_{\ell s}$	(8)
enthalpy transfer:	$H_{\ell s} = h_c(T_\ell - T_s)$	(9)
heat flux:	$\mathbf{q}_i = \alpha_i \nabla h_i$	(10)

The important novelty of this model is the implementation of the viscoplastic regime, which is imposed when $g_s > g_s^t$. The change in material behavior is transmitted through the effective deviatoric stress tensor included in equation (2), which is defined differently depending on whether the solid fraction is in the viscoplastic regime.

Below the viscoplastic threshold, the equation is defined by the general Newtonian viscous stress tensor ($\boldsymbol{\Sigma}_s^{eff} = \boldsymbol{\tau}_s = 2\mu_s \text{dev}(\dot{\boldsymbol{\varepsilon}}_s)$). This expression is analogous to the one adopted in the liquid phase with the strain rate tensor being defined as $\dot{\boldsymbol{\varepsilon}}_i = 1/2\left(\nabla \mathbf{v}_i + (\nabla \mathbf{v}_i)^T\right)$. The solid viscosity is expressed according to the power-law viscosity model of Ishii [10]. Assuming the validity of the mixture rule, it yields:

$$\mu_s = \mu_\ell / g_s \left(\left(1 - g_s / g_s^p\right)^{-2.5 g_s^p} - (1 - g_s) \right) \tag{11}$$

where the packing limit is set as $g_s^p = 0.585$, according to the loose random packing of spheres proposed by Olmedilla *et al.* [11].

In the viscoplastic regime, on the other hand, experimental studies on the behavior of metallic alloys at high temperatures show that the effective deviatoric stress tensor of the solid phase can be described by the following expression [7]:

$$\boldsymbol{\Sigma}_s^{eff} = \frac{\mu_s^{\text{app}}}{g_s}\left(\frac{2}{A}\text{dev}\left(\dot{\boldsymbol{\varepsilon}}_s\right) + \frac{1}{9B}\text{tr}(\dot{\boldsymbol{\varepsilon}}_s)\mathbf{I}\right) \tag{12}$$

where A and B are two rheological parameters proposed by Nguyen *et al.* [7], which affect the deformability of the mush in pure shear and hydrostatic states, respectively. They can be written as follows:

$$A = \frac{3}{g_s^{6.47}} \text{ and } B = \frac{1}{g_s^{6.94}} - 1 \tag{13}$$

and the apparent solid viscosity takes the form of the Norton-Hoff model:

$$\mu_s^{app} = 3K_v\left(\sqrt{3}\dot{\boldsymbol{\varepsilon}}_s^{eq}\right)^{m-1} \tag{14}$$

In the above expression, the apparent solid viscosity can be seen to depend on the equivalent strain rate, which is given by the following expression:

$$\dot{\varepsilon}_s^{\text{eq}} = \sqrt{\frac{2}{A}(\dot{\boldsymbol{\varepsilon}}_s : \dot{\boldsymbol{\varepsilon}}_s) - \left(\frac{2}{3A} - \frac{1}{9B}\right)\text{tr}(\dot{\boldsymbol{\varepsilon}}_s)^2} \tag{15}$$

which is again function of the rheological parameters defined in equation (13). The quantities K_v and m presented in equation (14) are the viscoplastic consistency and the strain-rate sensitivity, respectively. The latter parameter is usually assumed as a fixed value which depends on the material properties. In the present work, it is set as 0.213. On the other hand, the viscoplastic consistency can be calculated by combining the strain-rate tensor proposed by Nguyen *et al.* [7] and the Norton-Hoff stress-strain-rate relation. It takes the value of 6.31×10^6 Pa s.

3. Results and discussion

In a previous work [8], a simple cavity test case was analyzed in terms of melt convection, crystals dynamics, and macrosegregation. A comprehensive picture of the flow dynamics was described and details concerning the flow inside the viscoplastic regime and the eutectic reaction were also discussed. However, although the semi-solid dynamics at high solid fractions could be captured by the model, no clear evidences of solute redistribution driven by densification or dilatation of the mush were detected. In the present manuscript, the setup has been altered so that further interactions between the solidifying structures take place. In addition, the present results are compared against the outcome of a simulation that contemplates a rigid solid body formulation instead of the viscoplastic regime.

A vertical column test case is simulated, as represented in figure 1. The setup is characterized by an intensified cooling region that is enforced by assuming a very high heat transfer coefficient (HTC) defined in a specific section of both vertical walls. This simple setup provides a good opportunity for experimental validation in the future.

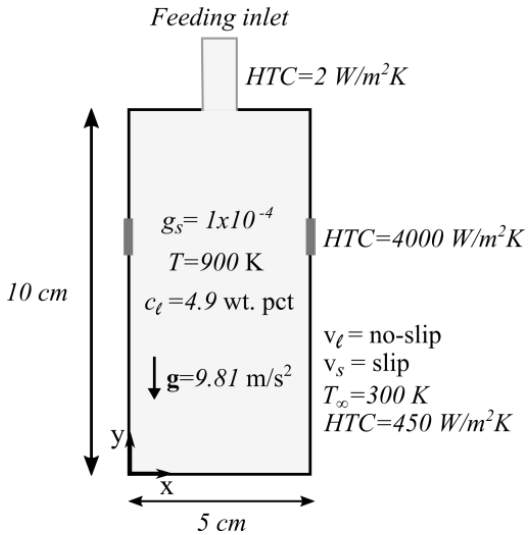

Figure 1. Schematic representation of the test case.

The presented simulation results are for an inoculated Al-5wt.%Si alloy. An inlet tube (with fixed pressure, $p = 10^5$ Pa) is designed so that shrinkage can be compensated by mass/liquid feeding. No-slip and slip boundary conditions are applied to the liquid and solid phases, respectively. Along the walls, a convection heat transfer boundary condition is imposed with a heat transfer coefficient (HTC) of 450 W/m^2/K along most of the walls, except at two locations. The first is along the feeding tube where HTC = 2 W/m^2/K so that almost no heat transfer is allowed along that portion of the wall. The second is in the already mentioned intensified cooling region where HTC = 4000 W/m^2/K (see figure 1). A very large heat transfer is adopted in this portion of the domain so that the two viscoplastic structures grow faster than elsewhere and eventually interact between each other during the solidification.

The simulation starts with a solid fraction of 1×10^{-4} (for computational reasons, a finite but very small value is considered), initial temperature of 900 K (liquidus line), and initial species concentrations of c_l = 4.9wt.% and c_s = 0.68wt.%. The present model only considers globular equiaxed crystals. The

solid and liquid densities are 2535 kg/m^3 and 2430 kg/m^3, respectively, and the constant liquid viscosity is taken as 1.09×10^{-3} kg/m/s. A two-dimensional orthogonal mesh with 50×100 cells is used (discounting the inlet tube). The simulation is performed with a variable time-step which remains in the order of 10^{-4} s a few moments after the start of the simulation.

Figure 2 illustrates the solidification and sedimentation of the Al-Si alloy, from a starting point where it is totally liquid (dark blue color). The feeding tube is not shown for simplicity and the black line signals the interface at which the viscoplastic model is triggered. Dark red regions correspond to eutectic structures. Initially, due to the slip boundary condition imposed to the solid phase, the equiaxed crystals immediately sink as they nucleate and grow. Because of the coupling between the two phases (through the momentum exchange term), the melt is also affected by the sinking crystals. This gives rise to a symmetric flow pattern with downward motion near the vertical walls and an upward motion at the center of the domain.

While the solid fraction is below the viscoplastic limit, the equiaxed crystals sink along the vertical boundaries and then, coming from both lateral walls, they collide at the bottom center of the domain. Once the viscoplastic regime is entered, the viscosity of the material increases substantially and the mush becomes stiffer. This can be seen near the walls in figure 2(a), where a coherent structure develops near the sides of the domain. Nevertheless, a more dynamic motion of the solid phase at lower solid fractions is kept between this two viscoplastic structures.

As the simulation proceeds, equiaxed crystals continue to sediment at the bottom and along the vertical walls (figure 2(b)). Once the stiffer formations reach the intensified cooling region (first near the walls), they provide a physical structure where the solid phase can accumulate. As a result, the crystals stop sinking immediately down and start to solidify also along the intensified solidification direction, i.e., towards the center of the domain (figure 2(c)). At the bottom, the coherent structure develops a strong curved interface as a result of the preferential accumulation of equiaxed crystals near the lateral walls and the established flow map [8].

With further solidification, the two separate structures that grow in the intensified cooling region start to approach each other near the center of the domain and, eventually, end up by forming a continuous coherent structure spanning the entire width of the domain (figure 2(d)). This generates an obstacle for the flow to move longitudinally. Notice also that a small region with solid fraction below the viscoplastic limit is still visible in the center of the configuration. In the last snapshot (figure 2(e)), the eutectic formations (dark red color) have merged at the center in the intensified cooling region, which at this point totally precludes the flow to move towards the bottom.

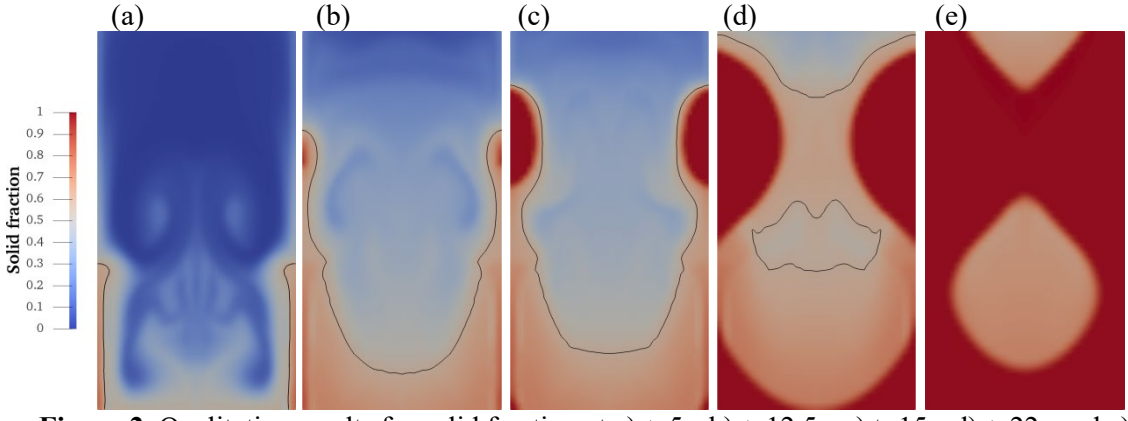

Figure 2. Qualitative results for solid fraction at a) *t*=5s, b) *t*=12.5s, c) t=15s, d) *t*=22s and e) *t*=28s.

While the two solidifying structures are separated, sedimentation and solidification feeding can progress from top to bottom with no substantial resistance, although macrosegregation deviations occur due to the induced cross-sectional change. However, once they approach each other, material has to flow

through the mush to feed solidification shrinkage at the bottom of the domain. While liquid feeding is generally expected, the viscoplastic formulation introduces a dynamic character to the solid phase that come into play here.

Figure 3 illustrates the vertical component of the solid velocity at t = 22 s. According to figure 2(d), it corresponds to a stage where a continuous viscoplastic structure extends between both vertical walls, and separates the solidifying material located at the bottom from the inlet located at the top. Although eutectic structures are identified near the sides, they still are separate enough to allow for material to flow along the centre. Furthermore, in figure 3, the results of the present model are compared against a simulation that considers the common simplification of assuming a rigid solid body (given by an arbitrary high constant solid viscosity) instead of the viscoplastic regime. The snapshot is divided in half longitudinally: the left half corresponds to the outcome of the current model, whereas the right half shows the outcome of the rigid solid body formulation.

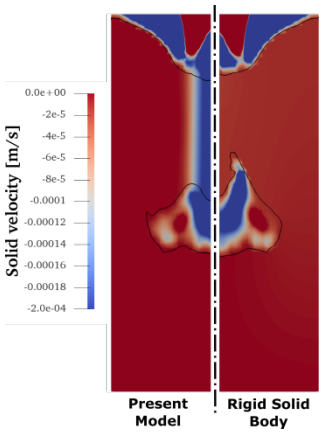

Figure 3. Vertical component of the solid velocity at t = 22 s for present model (left half) and rigid solid body formulation (right half).

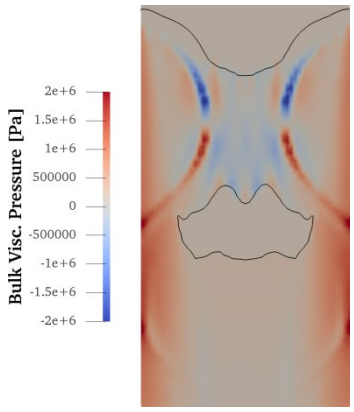

Figure 4. Calculated pressure induced by the bulk viscosity term in the viscoplastic regime at t = 22 s. The red color corresponds to dilatation of the mush, whereas the blue color corresponds to densification.

Because the solid viscosity in the viscoplastic regime is dynamic (i.e. it depends on the strain rate and solid fraction, as shown in equations (13) to (15), the downward solid velocity through the mush also varies across the horizontal cross section of the intensified cooling region. Interestingly, the maximum absolute solid velocity (found in the centre) is of the same order of magnitude as the liquid velocity in that region. This downward flow only occurs in the viscoplastic region, whereas in the eutectic structure the solid velocity is essentially zero. On the other hand, in the rigid solid body formulation, the velocity is roughly non-existent (dark red color in the snapshot) across the whole width of the domain. These results suggest that in the latter approach, the solidification taking place at the bottom of the domain is fed purely with melt (liquid feeding), whereas in the present model the solid phase also contributes to feed solidification (mass feeding).

Such mechanism is the results of a dynamic viscosity assumed in the viscoplastic regime but is also driven by the extra solid pressure that is derived from the second term on the right-hand side of equation (12). This latter quantity is shown in figure 4 at t = 22 s (referred in the results as the bulk viscosity pressure). Dilatation of the mush is observed in the lower part of the solidifying viscoplastic mush, which means that additional melt is drawn to this area. As a consequence, further material has to compensate for the solidification feeding, which comes not only as liquid but partly also in the form of solid phase (as indicated by the previous figures).

For reference, the largest absolute values found in figure 4 are roughly one order of magnitude larger than the shared pressure across the domain (in absolute terms) during most of the simulation. This

finding highlights the significance of such parameter in the results, even though it only appears at very specific locations where densification or dilation occurs. Nevertheless, it is important to emphasize that the shared pressure field is also highly influential on the flow dynamics.

Although not directly shown here, the pressure field has been found to be an important driving force for the solidification-driven feeding flow, with larger pressure gradients along the vertical axis being observed as the feeding difficulties increase during that process. However, right after the two eutectic structures form a continuous solid structure in figure 2(e), the lower limit of the pressure field rapidly drops to around 10 kPa. In reality, this scenario would most probably lead to feeding related defects, such as porosity, and hot-tearing formations, as their appearance has been associated with large pressure drops at the end of the casting processes [12, 13]. In the simulation, however, since such mechanisms are not accounted for in the present model and the feeding flow through the solidified material becomes practically impossible, the simulation ends up by crashing.

The present results have shown the presence of local dilatation of the mush in certain regions. This leads to an additional inflow of melt that supplements the feeding flow necessities required to compensate solidification shrinkage. However, besides the melt, also solid feeding has been observed during relevant stages of the simulation. These findings have both a direct effect on the relative motion between the phases, which eventually affects the composition deviation of the alloy. Figure 5(a) illustrates the macrosegregation formation at t = 22s across the domain for both the present model and the rigid solid body formulation. Qualitatively, similar distributions can be seen. This means that the rigid solid body formulation might be employed in test cases where a simple estimation of the composition deviations is needed.

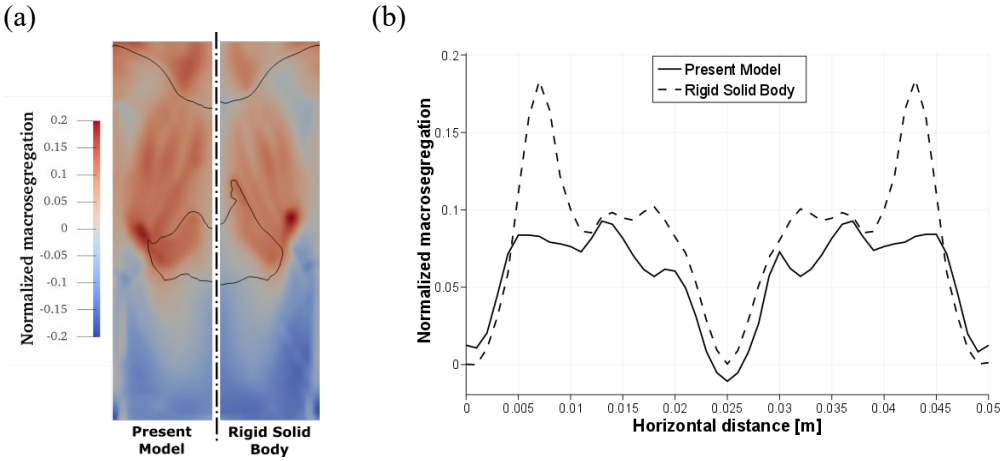

Figure 5. (a) Normalized macrosegregation (c_{mix}/c_0-1) distribution for present model (left half) and rigid solid body model (right half) at t = 22 s. (b) Quantitative results for normalized macrosegregation along a horizontal line located in the middle of the domain.

However, in quantitative terms, some discrepancies can be identified. Figure 5(b) presents the composition deviation along a horizontal line located in the middle of the domain. It exhibits a significant positive deviation spike in the rigid solid body formulation at x=0.007m and x=0.043m, whereas the present model presents a more uniform distribution in this region (due to the reasons discussed above). Both models have a slight negative deviation along the centerline mostly because the inflow of melt to feed solidification in this area mainly comes from the inlet, which possesses the initial melt composition. Therefore, although the general macrosegregation distribution looks similar, the extra complexity of the viscoplastic regime ends up by stabilizing the spikes observed in the macrosegregation results.

4. Conclusion

In the present paper, a comprehensive model has been described that can be employed to simulate the entire solidification process. A simple test case has been devised so that solidifying structures strongly interact with one another and impose obstacles to the solidification-driven feeding flow across the domain. The simple setup has been considered so that it can be replicated experimentally for proper validation of the computational results.

The results show that the viscoplastic regime employed in the present formulation provides for a more dynamic version of the solid phase, even for high solid fractions. Besides the expected liquid feeding, mass feeding has also been observed in a scenario where a strong inflow was required. The results contrasted with the common general rigid solid body formulation, which completely neglects such mechanism. Also, areas of densification and dilatation have been observed, which influenced the flow behavior during the simulation. Such mechanisms provide for more active relative motion between the phases, which end up by affecting the final macrosegregation formations.

Acknowledgments

This work was financially supported mainly by the FWF Austrian Science Fund (P28785-N34), and by the Austrian Federal Ministry of Economy, Family and Youth and the National Foundation for Research, Technology and Development within the framework of the Christian Doppler Laboratory for Metallurgical applications of Magneto-hydrodynamics.

References

[1] Guazzelli E and Pouliquen O 2018 *Journal of Fluid Mechanics* **852** 1-62
[2] Drezet J M, Mireux B, Szaraz Z and Pirling T 2014 *Miner.* Met. Mater. Soc. **66** 1425–30
[3] Martin C L, Favier D and Suéry M 1999 *Int. J. Plast.* **15** 981–1008
[4] Geindreau C and Auriault J L 1999 *Mech. Mater.* **31** 535–51
[5] Rodrigues C M G, Ludwig A, Wu M, Kharicha A and Vakhrushev A 2019 *Metall. Mater. Trans. B* **50** 1334–50
[6] Fachinotti V D, Le Corre S, Triolet N, Bobadilla M and Bellet M 2006 *Int. J. Numer. Methods Eng.* **67** 1341–84
[7] Nguyen T G, Favier D and Suery M 1994 *Int. J. Plast.* **10** 663–93
[8] Rodrigues C M G, Ludwig A, Wu M, Kharicha A and Vakhrushev A *Computational Materials Science* (submitted)
[9] Greenshields C J, OpenFOAM – The OpenFOAM Foundation – User Guide, 2018. http://foam.sourceforge.net/docs/Guides-a4/Op enFOAMUserGuide-A4.pdf
[10] Ishii M 1977 *Report No. 77-47* (Argonne National Laboratory, ANL, Illinois)
[11] Olmedilla A, Zaloznik M and Combeau H 2017 *Powders and Grains 2017* **140** 1-4
[12] Eskin D G and Katgerman L 2007 *Metall. Mater. Trans. A* **38** 1511–9
[13] M'hamdi M, Mo A and Martin C L 2002 *Metall. Mater. Trans. A* **33** 2081–93